Hindawi
Journal of Engineering
Volume 2024, Article ID 8232145, 15 pages
https://doi.org/10.1155/2024/8232145

Research Article

Study on the Safety Thickness of Three Zones against Fault Water Inrush: Case Study and Model Development

Yongqian Wang,[1] **Benshui Yang**,[2] **and Jun Zhang**[3]

[1]*School of Architecture and Engineering, Qingdao Huanghai University, Qingdao 266427, China*
[2]*School of Civil Engineering, Anhui Jianzhu University, Hefei 230022, China*
[3]*China Construction Sixth Engineering Bureau Limited, Tianjin 300451, China*

Correspondence should be addressed to Yongqian Wang; wangyq02@qdhhc.edu.cn

Received 5 August 2023; Revised 29 October 2023; Accepted 5 December 2023; Published 9 January 2024

Academic Editor: Andras Szekrenyes

The raising and flowing of groundwater caused by coal mining threaten the stability of mining faces, which cause casualties and machine damage accidents. Among the above accidents, the water inrush disaster caused by the water-rich water-conducting fault zone is the largest. Considering the complexity of geological structure and the suddenness of water inrush, reserving a reasonable thickness of waterproof coal pillars in front of the fault tectonic belt can effectively predict and control the occurrence of water inrush. The excellent adaptability of the numerical model to the geological conditions makes it an effective research method for simulating waterproof coal pillars. Based on the analysis of the background of on-site mining, this paper proposes a three-zone waterproof coal pillar calculation theory and establishes a numerical model for comparative analysis. The comparison results show that (1) the elastic-plastic theory and fracture theory can be used to calculate the thickness of the disturbed zone and the water-resisting zone, and the thickness of the fractured zone is positively correlated with the accuracy of the existing detection technology and equipment. (2) For the numerical model results, the increase of tangential stress is positively correlated with the distance of coal seam mining and the thickness of fault; the large plastic zone of the fault causes a higher increase in pore pressure, which ultimately increases the risk of water inrush. (3) The two results are in good agreement. The theoretical results have a safety margin, indicating that the three-zone theory is reasonable, which are used to guide the actual mining of the project to ensure the smooth passage of the project through the fault area.

1. Introduction

When underground coal seam mining encounters faults with complex structure, low strength, and instability under external interference, it is easy to cause collapse, roof caving, and water seepage accidents [1–5]. In particular, when mining on a confined aquifer, high water pressure and stress redistribution activate existing faults and further improve the permeability of faults; thus, the water inrush channel is formed by a groundwater conduction fault, in which a significant amount of confined water can suddenly invade the mining face [6–8]. The risk and casualty of water inrush disasters have increased due to the existence of faults [9, 10], and more than 10000 deaths have occurred due to water inrush accidents worldwide [11, 12]. Therefore, it is of great theoretical significance to study the fault activation and water conduction mechanism to prevent the occurrence of water inrush accidents.

It is widely recognised that both water pressure and mining activities have considerable influences on fault activation [13–15]. The stress redistribution resulting from the underground mining process exerts an enormous influence on the stress state of nearby rock masses, which could lead to a decrease in the principal stress on regional faults [16, 17]. Meanwhile, the original crack propagation of the rock mass in a fault further reduces the stress intensity of the rock mass and becomes a new path for hydraulic migration [18–20]. Furthermore, the development of the failure

zone formed by coal seam mining breaks over the hydraulic crack zone of the fault, which indicates that a water inrush channel is formed [21–23]. In addition, mining height also has an important influence on water inrush in underground mines where faults are present. Therefore, many numerical analyses of mining models, including fault-water geological structures, have been employed by scholars to solve the problem, for instance, finite element and discrete element methods [8, 24–29]. Among these studies, the conclusions about fault water inrush obtained by the FLAC3D software are important for understanding the mechanical properties of faults [12, 30–33]. Furthermore, few theories consider the water pressure, as well as the waterproof coal pillar in the process of coal seam excavation. In order to better understand the problem of fault water inrush encountered in underground mining, it is necessary to incorporate the mechanism of fault action into the simulation of coal mining.

Based on the field monitoring data and geological conditions, this paper aims to quantitatively evaluate the influence of fault size and water content on the width of waterproof coal pillar in coal seam mining activities by combining numerical model analysis with theory. The width acquired within the theoretical approach is then quantitatively compared to that of the FLAC3D model and other approaches estimated from mining engineering regulations, which help to gain useful insight into the mechanical properties of the faults and to provide knowledge about the numerical simulation of waterproof coal pillar retaining.

2. Engineering Background

The Wugou Mine is located 50 km southwest of Huaibei city, Anhui Province, China, covering a minable area of approximately 15 km^2. There are multiple coal seams in the mining area, and the thickness of the #10 coal seam is 3.95 m with a burial depth of 450 m. A large compressive normal fault F14 tends to the NW, with an inclination angle of 70°, a drop between 10 and 380 m, and an extension length greater than 4300 m. The roof of the #10 coal seam is a medium and silty sand composite stratum, the floor is sandstone and mudstone, and the limestone of the Taiyuan Formation is an aquifer. The Wugou coal mine is mainly affected by the fourth aquifer of the Cenozoic, and the water pressure at the bottom of the #10 coal seam is 2.6 MPa. During the mining of the #1011 working face, the water inflow in the goaf is expected to be 35 m^3/h. Thus, it is necessary to evaluate the degree of confined water inrush near-fault F14 and consider a reasonable coal pillar height. The geological structure map and geological profile of the Wugou mine field are shown in Figure 1, and Table 1 shows the physical and mechanical properties of roof and floor strata in coal seams.

3. Theoretical Content Results

3.1. Model of Three-Zone Calculation Theory. The strata between the mining face and the fault are divided into three parts: the influence area of construction disturbance, the main water-resisting area, and the water pressure fracture area. The mechanical model diagram is shown in Figure 2.

3.2. Construction Disturbance Influence Area h_1. The failure zone of the rock mass at the edge of the excavation face under the plane stress state is larger than that of the plane strain state, and the failure domain under the plane strain state considering stress relaxation is close to that of the plane stress state. Therefore, in practical applications, the range of the failure zone of the surrounding rock edge of the mining face is calculated according to the plane strain of the stress relaxation. The mining section is circular, and the rock mass is assumed to be isotropic, continuous, and homogeneous. Based on the two-way compression plate of elastic theory, the plane strain state at a point on the centre line of the mining face is analysed, as is shown in Figure 3.

3.2.1. Stress State Analysis. According to Chelsea's answer in elasticity theory, we get the following equation:

$$\left.\begin{aligned}
\sigma_r &= \frac{\sigma_1+\sigma_3}{2}\left(1-\frac{a^2}{r^2}\right)+\frac{\sigma_1-\sigma_3}{2}\left(1-\frac{a^2}{r^2}\right)\left(1-3\frac{a^2}{r^2}\right)\cos 2\theta,\\
\sigma_\theta &= \frac{\sigma_1+\sigma_3}{2}\left(1+\frac{a^2}{r^2}\right)-\frac{\sigma_1-\sigma_3}{2}\left(1+3\frac{a^4}{r^4}\right)\cos 2\theta,\\
\tau_{r\theta} &= \frac{\sigma_1-\sigma_3}{2}\left(1-\frac{a^2}{r^2}\right)\left(1+3\frac{a^2}{r^2}\right)\sin 2\theta,
\end{aligned}\right\}, \tag{1}$$

where σ_r and σ_θ are the radial and circumferential normal stresses, respectively; $\tau_{r\theta}$ is the shearing stress; σ_1 and σ_3 are the maximum and minimum principal stresses, respectively; a is the excavation radius; and r and θ are the distance and included angle from point B to the centre, respectively. Set the lateral pressure coefficient of the surrounding rock as follows:

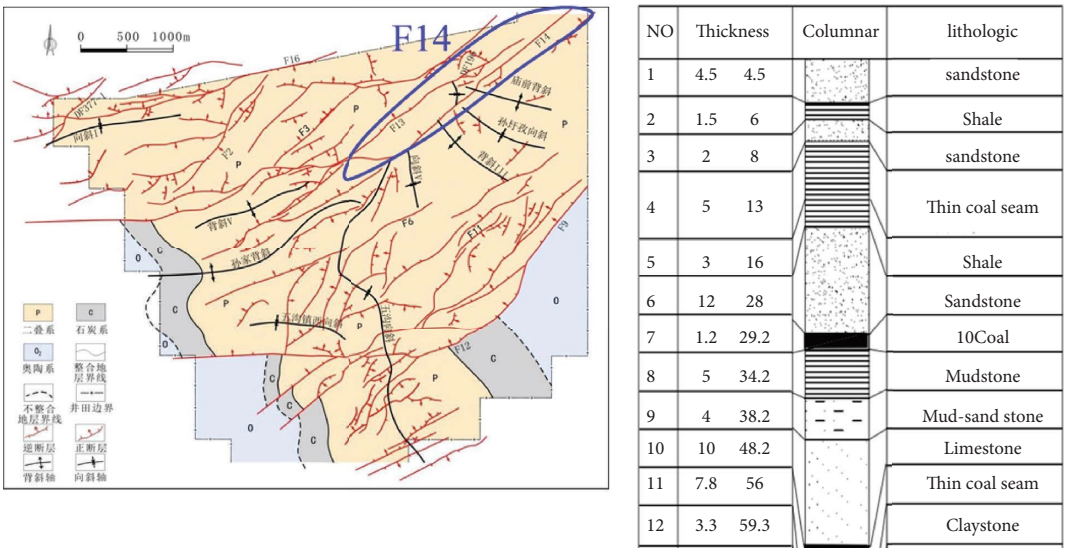

(a) (b)

Figure 1: Geological fault structure map and geological profile of the Wugou mine. (a) General geology. (b) Geological profile.

Table 1: Physical and mechanical properties of rock.

Lithology	μ	E (GPa)	ϕ (°)	C (MPa)	R_c (MPa)	ρ_v (KN·m^{-3})
Medium sand	0.22	38	30	8.65	33	27.9
Fine sandstone	0.18	45	35	4.75	44	26.5
Siltstone	0.25	26	32	2.37	34	25.4
#10 coal	0.27	18	28	2.1	11	14.0
Mudstone	0.23	20	32	2.03	28	25.0
Limestone	0.23	66	30	4.5	35	26.6
Mud-sandstone interbedding	0.22	29	31	3.7	30	26.4

$$\left.\begin{aligned} \sigma_3 &= \gamma\sigma_1, \\ \gamma &= 1. \end{aligned}\right\},$$

$$\left.\begin{aligned} \sigma_r &= \sigma_1\left(1-\frac{a^2}{r^2}\right), \\ \sigma_\theta &= \sigma_1\left(1+\frac{a^2}{r^2}\right), \\ \tau_{r\theta} &= 0, \end{aligned}\right\}, \tag{2}$$

where each parameter has the same meaning as in equation (1).

At this point, the elastic stresses near the circular excavation face are shown in Figure 4.

As shown in Figure 4, the principal stress difference around the excavation face is the largest, so is the shear stress. The deformation and failure begin to develop gradually from the periphery of the excavation face to the depth of the surrounding rock. The thickness of the plastic zone is used as the thickness of the rock layer in the fracture zone.

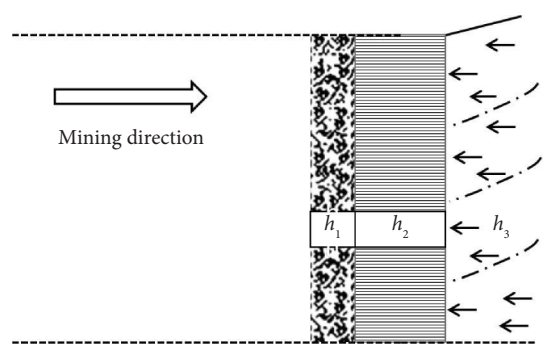

Figure 2: Three-zone calculation model.

3.2.2. Stress Distribution of Inelastic Deformation Zone. Based on the Mohr–Coulomb failure criterion, we get the following equation:

$$\left.\begin{aligned} \sigma_r &= (P_t + c\cot\varphi)\left(\frac{r}{a}\right)^{2\sin\varphi/1-\sin\varphi} - c\cot\varphi, \\ \sigma_\theta &= (P_t + c\cot\varphi)\left(\frac{1+\sin\varphi}{1-\sin\varphi}\right)^{2\sin\varphi/1-\sin\varphi} - c\cot\varphi, \end{aligned}\right\}, \tag{3}$$

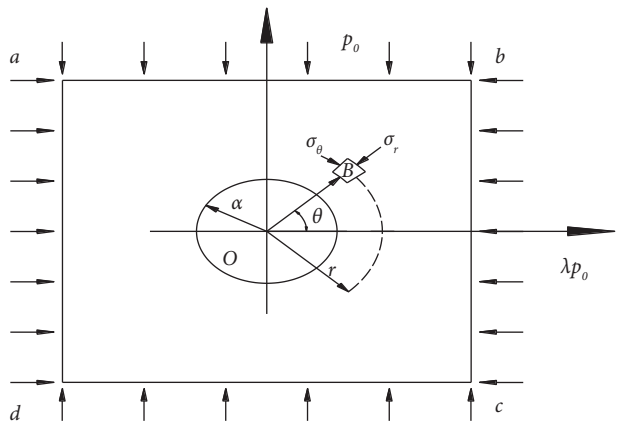

Figure 3: Plane stress state of the excavation face.

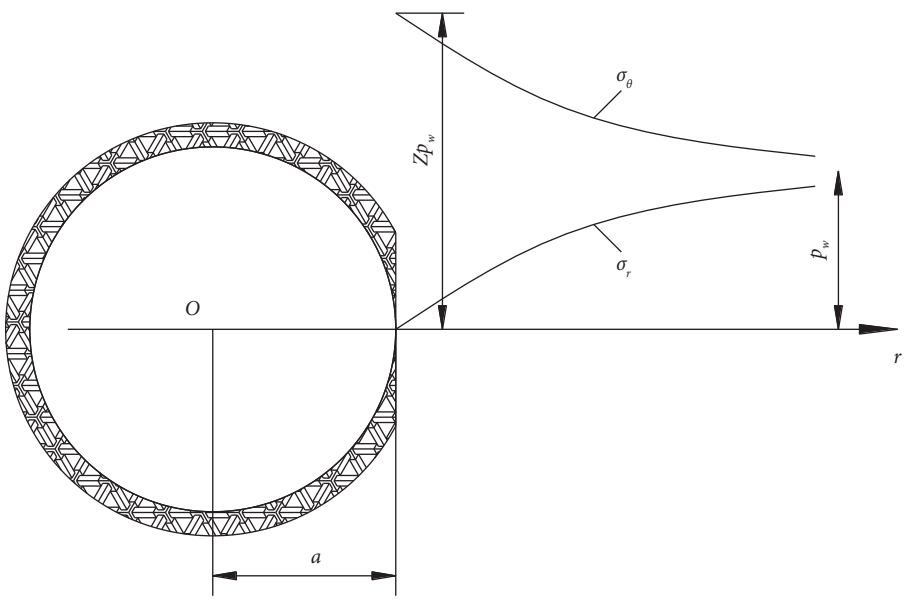

Figure 4: Radial and circumferential stress distribution around the excavation face.

where c and ϕ are the cohesion and friction angle of the rock stratum, P_t is the support reaction force, and the other parameters have the same meaning.

Plastic Zone of Circular Mining Face. H. Kastner proposed that the plastic failure zone of roadway excavation is a circular plastic zone around the roadway, and its calculation formula is as follows:

$$h_1 = R = a\left[\frac{(P_0 + c\cot\varphi)(1 - \sin\varphi)}{P_t + c\cot\varphi}\right]^{1-\sin\varphi/2\sin\varphi}, \quad (4)$$

where the meaning of each parameter in the formula is the same as in the above equations.

3.3. Main Water-Resisting Zone h_2. Affected by mining activities, the stress release of the main water-resisting strata reduces the ability of the rock to resist the splitting of the surrounding fissure water, resulting in the growth and even penetration of the original cracks in the strata, and the splitting failure causes water inrush.

3.3.1. Initiation and Propagation of Fracture. When brittle failure occurs in closed cracks, the stress concentration at the crack tip leads to crack propagation and failure, which is shown as follows:

$$\left.\begin{aligned} &(\sigma_1 - \sigma_3)^2 - 8R_t(\sigma_1 + \sigma_3) = 0, (\sigma_1 + \sigma_3 \geq 0), \\ &\sigma_3 = -R_t, \text{others}, \end{aligned}\right\}, \quad (5)$$

where R_t is the tensile stress and the other parameters have the same meaning.

The compressive stress required for fracture closure is very small, which can be negligible, and the equation can be simplified as follows:

$$\sigma_1\left[\left(f^2+1\right)-f\right]-\sigma_3\left[\left(f^2+1\right)-f\right]=4R_t, \tag{6}$$

where f is the coefficient of friction and the other parameters have the same meaning.

3.3.2. Thickness of the Hydraulic Fracturing Zone. When the mining is advancing to a certain distance, the critical water pressure of the hydraulic fracturing of strata is reached, and fracture failure of the face is about to occur.

According to the D-B model of the plastic zone, the size of the plastic zone is determined by the stress state at the crack tip. When the stress intensity factor at the crack tip is zero, the size of the plastic zone is obtained as follows:

$$r_p=a\left(\sec\frac{\pi\sigma^{\infty}}{2\sigma_0}-1\right), \tag{7}$$

where r_p is the radius of the plastic zone, σ_0 is the initial stress, and a is the excavation radius.

Under the small-scale yield, we get the following equation:

$$\frac{\sigma^{\infty}}{\sigma_0}\ll 1. \tag{8}$$

Expand the formula in a Taylor series as follows:

$$r_p=\frac{a}{2}\left(\frac{\pi\sigma^{\infty}}{2\sigma_0}\right)^2+\frac{5a}{24}\left(\frac{\pi\sigma^{\infty}}{2\sigma_0}\right)^4+\ldots, \tag{9}$$

where the parameters have the same meaning as in equation (7).

The first item was choosen only as follows:

$$r_p=\frac{a}{2}\left(\frac{\pi\sigma^{\infty}}{2\sigma_0}\right)^2=\frac{\pi}{8}\frac{K_{\mathrm{II}}^2}{\sigma_0^2}, \tag{10}$$

where K is the stress intensity factor and the other parameters have the same meaning as in equation (7).

The same application of the above formula was performed under large yield conditions. The stress state of the surrounding rock crack during hydraulic fracturing is as follows:

$$\left.\begin{aligned}\sigma_0&=\frac{\sigma_1+\sigma_3}{2}-\frac{\sigma_1-\sigma_3}{2}\cos 2\beta-P_w,\\ \tau_0&=\frac{\sigma_1-\sigma_3}{2}\sin 2\beta,\end{aligned}\right\}, \tag{11}$$

where σ_0 and τ_0 are the normal stress and shear stress of rock under water pressure, respectively; σ_1 and σ_3 are the maximum and minimum principal stresses, respectively; β is the friction angle of rock under water; and P_w is the critical water pressure under tension or compression-shear stress, which is expressed as follows:

$$\begin{aligned}P_w=&\frac{\sigma_1-\sigma_3}{2}-\frac{\sigma_1+\sigma_3}{2}\left(\cos 2\beta+\frac{\sin 2\beta}{\tan\varphi}\right)\\&-\frac{c+K_{\mathrm{II}}\left(\sqrt{3\pi a}/2\pi a\right)}{\tan\varphi},\end{aligned} \tag{12}$$

where the parameters have the same meaning as before. It can be obtained as follows:

$$h_2=r_p=\frac{\pi}{8}\frac{K_{\mathrm{II}}^2}{\sigma_0^2}=\frac{\pi}{2}\frac{K_{\mathrm{II}}^2}{\left[\left(\sigma_1+\sigma_3\right)-\left(\sigma_1-\sigma_3\right)\cos 2\beta-2P_w\right]^2}, \tag{13}$$

where the parameters have the same meaning as in equation (12).

3.4. Rock Thickness in Fracture Zone h_3. Due to the complex nature of rock fractures around the fault, drilling or geophysical prospecting methods are used to obtain a more detailed evaluation of groundwater erosion of rock strata during the excavation of rock strata. The hydraulic characteristics of rock strata in front of mining are obtained by integrating the advanced prediction method of the geological radar. The detection results are used as the thickness value of the rock strata in the fracture area.

3.4.1. The Water-Rich Exploration of the F14 Fault. The transient electromagnetic method (TEM) is used to detect water abundance in the F14 region, and the water abundance in the detection area is shown in Figure 5. The purple virtual frame area is a water-rich area, and the length of water-rich area between fault and coal seam is 2.6 m.

3.4.2. Fault Information Revealed by Gallery and Ground Drilling. The profile results of fault drilling are shown in Figures 6 and 7 and Table 2. From Table 2, it can be seen that the length of water-rich fracture zone is 1.3 m.

3.5. Comparison of Theoretical and Experimental Results. The waterproof rock layer reserved thickness can be expressed as follows:

$$h=h_1+h_2+h_3. \tag{14}$$

The values of each parameter are shown in Table 3.

The reasonable coal pillar thickness obtained from the failure theory of the three zones is 30.6 m. The width of the fault waterproof coal pillar obtained by the theoretical method is more in line with actual mining than with similar test results. However, more verification methods are needed, such as numerical simulations, theoretical comparisons, and example verification, to further determine the adaptability of the three zones theory.

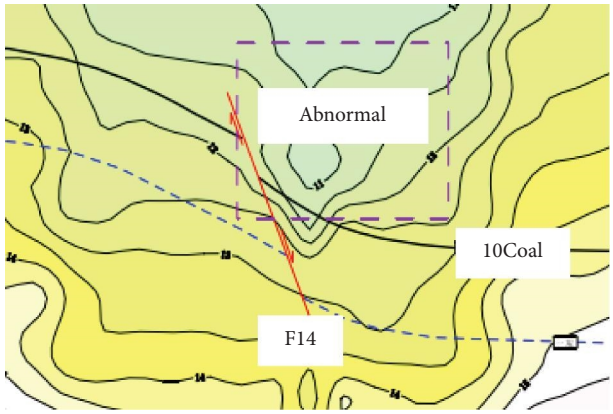

Figure 5: TEM detection results of F14.

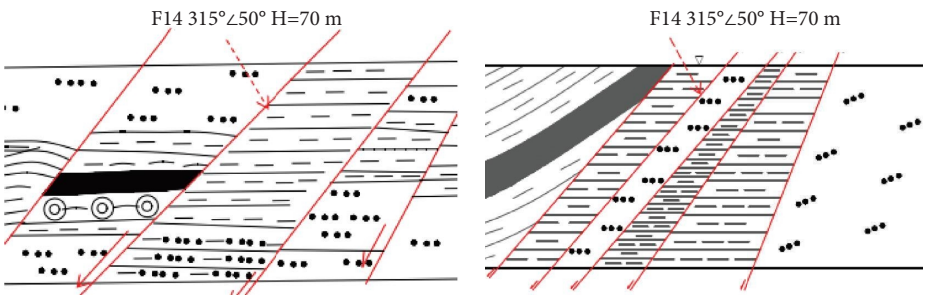

(a) (b)

Figure 6: Geological profile of roadway detection. (a) −380 m south wing taper. (b) South-10 return air roadway.

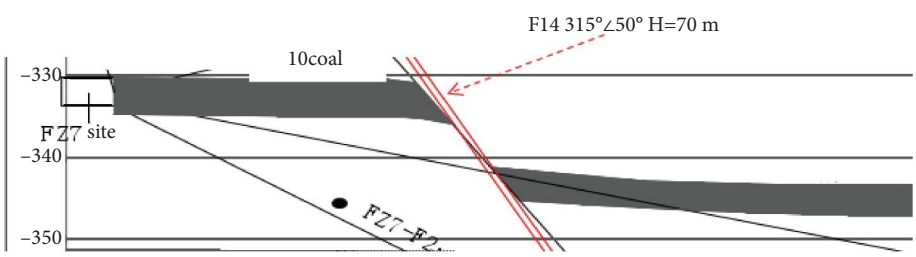

Figure 7: F14 profile of drilling exploration.

Table 2: Drilling and roadway exploration results of F14.

Type	No.	Thickness (m)			Lithologic characteristics	Water diversion
		Fault	Hanging wall	Footwall		
Drilling	80-2	7.29	0.17	2.42	Limestone-coal	Moderate
	30-1	7.58	2.69	1.17	Mudstone, #10 coal	Feeble
	1012-1	4.07	1.99	2.34	Mudstone	Feeble
	F23	17	4.3	2.8	Mudstone, siltstone	Moderate
	F27	10.8	0.5	5.8	#10 coal, limestone	Strong aqueous
Gallery	South-10	70	1.5	1.8	Sandstone, mudstone	Moderate
	−380 m	70	2.3	2.2	Siltstone, mudstone	Feeble
TEM exploration		Approximately 10 m			Strong aqueous under the coal connection	

Table 3: Calculation parameters of three-zone theory.

Partition	c (MPa)	ϕ (°)	P_t (MPa)	P_0 (MPa)	a (m)	σ_1 (MPa)	σ_3 (MPa)	K_{II} (MPa $*$ m$^{1/2}$)	β (°)
h_1	0.18	30	1.18	0.8	1.8	—	—	—	—
h_2	—	—	—	—	—	24.8	10.4	Experiment determination	30
h_3	—	—	—	—	—	—	—	—	—

4. Numerical Model Validation Method

4.1. Numerical Modelling. The FLAC-3D finite difference software was used to study the characteristics of water inrush and the reasonable safety width of the coal pillar. This simulation adopts the Mohr–Coulomb criterion of an ideal elastic-plastic rock mass. As shown in Figure 8, the size of the established 3D numerical model is 800 m (length) × 300 m (width) × 144 m (height), and the fault dip angle is 70°, which was used to simulate the length of 150 m fully mechanized 1011 mining face in Wugou Mine. The simulated actual formation conditions are shown in Table 1.

The boundary conditions of the model are the horizontal constraint around the model, the fixed constraint at the bottom, and the free boundary of the upper surface.

In this simulation, the overburden load is optimised to a uniform load, and the calculation parameters are selected in Table 4.

4.2. Results of Numerical Simulation

4.2.1. Variation Law of the Overburden Stress Field. Figure 9 shows the change in shear stress and vertical stress of the overlying rock with fault widths of 5 m, 8 m, and 12 m when the mining advances 90 m.

Figure 10 shows the change in shear stress and vertical stress of the overlying rock when the mining advances 210 m, 150 m, and 30 m.

As the advancing distance increases, the vertical stress and shear stress increase slowly. Under the same advancing distance, the shear stress of the overlying strata has a positive correlation with the increase in fault width, while the growth in vertical stress is the opposite. For example, when coal seam mining reaches a fault depth of 90 cm, the vertical stress caused by the fault fracture zone with widths of 5 m, 8 m, and 12 m is 39.791 MPa, 39.342 MPa, and 38.852 MPa, and the maximum shear stress is 8.603 MPa, 8.618 MPa, and 8.632 MPa. The changes in shear stress and vertical stress with the mining advance distance under three fault widths are shown in Figure 11.

The time and stress curves of the other two faults (5 m and 8 m) are shown in Figure 12. The increase of shear stress and normal stress is proportional to the distance between the excavation face and the fault. When the excavation distance reaches T0, the stress growth curve changes from gentle to sharp.

4.2.2. Variation of the Plastic Zone. Figure 13 shows the plastic strain range zone of the 5 m fault with the advance of the mining distance. It is shown that with the development of mining, the plastic zone is expanding accordingly. The roof and floor of the mined-out area are tensile-shear stress zones. At this distance, the roof is shear stress, and the floor is a tensile stress zone. When the distance between the mining face and fault is 30 m, the shear stress in the fault is obvious.

Figure 14 shows the plastic zones of 8 m and 12 m faults at 30 m distances under mining faces and faults. It is shown that with the same mining distance, there is much similarity in the range of the plastic strain zones in the goaf of the models with 8 m and 12 m faults, and the shear stress zone of the fault first appears in the lower plate position, which is shown in the red line section. The range of the plastic zone decreases and shear stress increases with increasing fault width, and at the same mining level, the footwall of the fault is in the state of compression and shear.

Figure 15 shows the displacement curves of the upper and lower plates at the same horizontal position under the width of the three fault fracture zones during the mining advance. It can be seen from Figure 15 that the vertical displacement increases step by step when mining advances to a certain position. Furthermore, the displacement of the upper plate is greater than that of the lower plate, where differences are expressed as d_1, d_2, and d_3. The vertical displacement of the upper and lower plates increases with increasing fault thickness, so is the difference between the upper and lower plates, that is, $d_1 < d_2 < d_3$. Moreover, for the upper side, the displacements of the 5 m, 8 m, and 12 m faults are 3.9 mm, 4.3 mm, and 4.8 mm, respectively.

4.2.3. Pore Water Pressure. Figure 16 shows the pore pressure of the 5 m fault under different propulsion distances. It is seen from Figure 16 that with the advance of the mining face to the fault, the pore pressure value increases continuously, which increases from 0.8 MPa to 1.7 MPa, and the maximum value appears at both ends of the goaf. When the mining advances to 30 m from the fault, the pore pressure in the fault increases to 0.4 MPa, which means water pressure is high, and seepage is considered to have occurred.

Figure 17 shows the pore pressure change cloud chart of the 8 m and 12 m faults for a 30 m distance between the mining face and fault. When the mining advances to 30 meters from the fault, with the increase in fault width, the water pressure in the fault is increasing, and the greater the growth range of water pressure is, the greater the possibility of water inrush. The fault becomes an important water inrush channel, which leads to underground aquifers and the mining face.

Figure 18 shows the pore pressure and flow velocity of the fault under different mining advances. It can be seen from Figure 18 that the pore water pressure increases

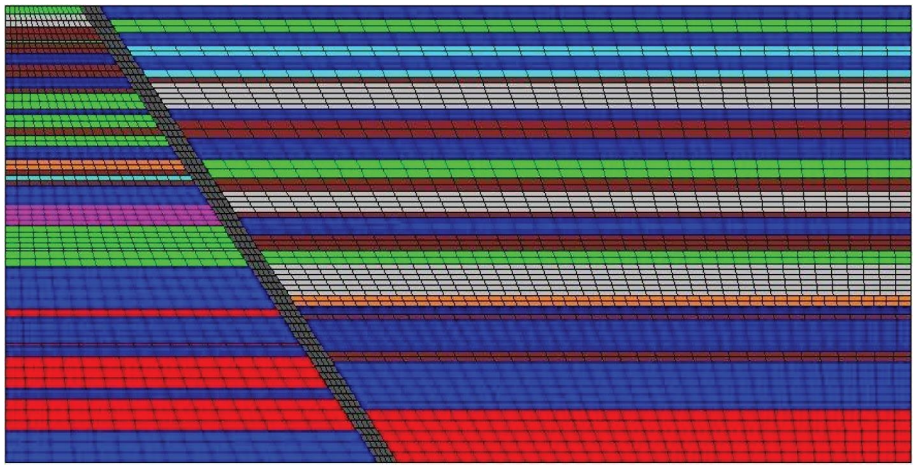

Figure 8: Model grid division.

Table 4: Rock mechanics parameters used in the numerical simulation.

Type	ρ (g·cm^{-3})	G (GPa)	ϕ (°)	f_c (GPa)	C (MPa)	f_t (MPa)
Fault	2.0	0.208	26	0.278	1.5	0.1
Rock	2.1	0.221	28	0.28	1.56	0.12

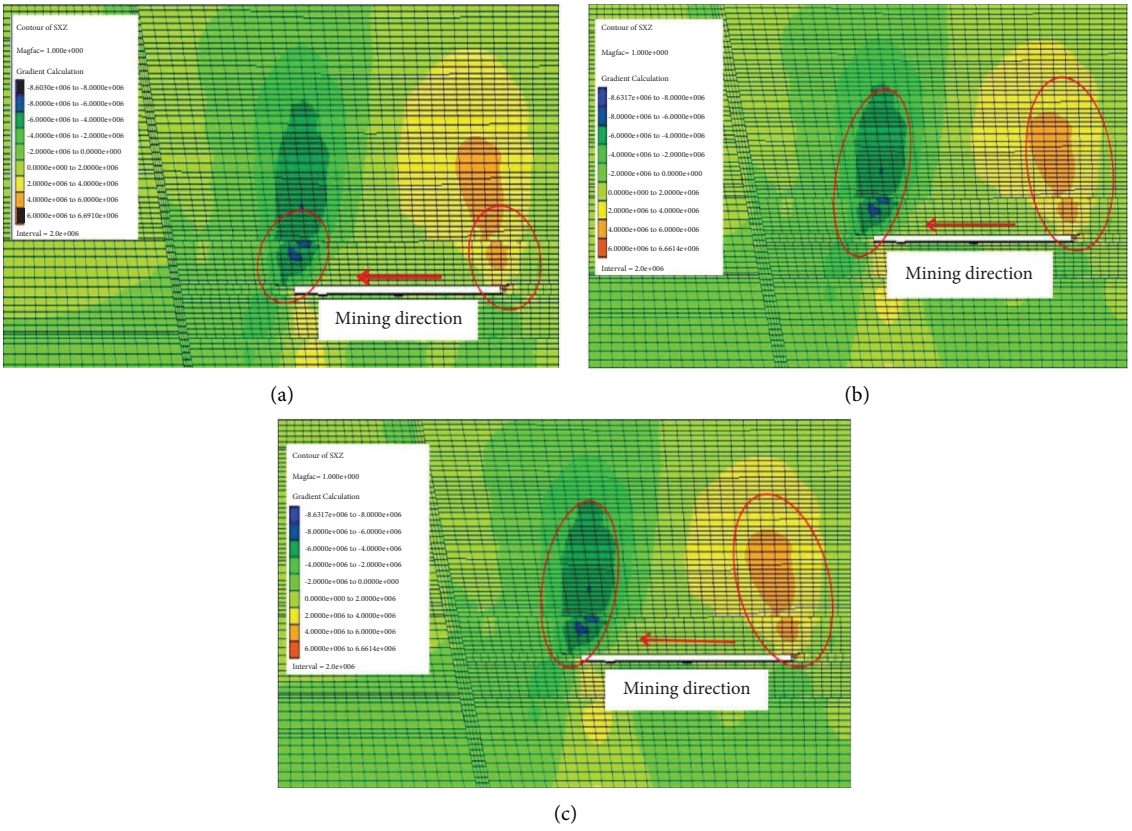

Figure 9: Shear stress nephograms under three fault thicknesses at a distance of 90 m under the mining faces and faults. (a) 5 m. (b) 8 m. (c) 12 m.

nonlinearly with mining distance and fault width, where peak value is 0.3 MPa when the mining distance is 30 m from the fault. Taking the inflection point of three pore pressure curves as the reference points H_1, H_2, and H_3 for determining the width of waterproof coal pillar can prevent further increase of pore pressure in fault F14.

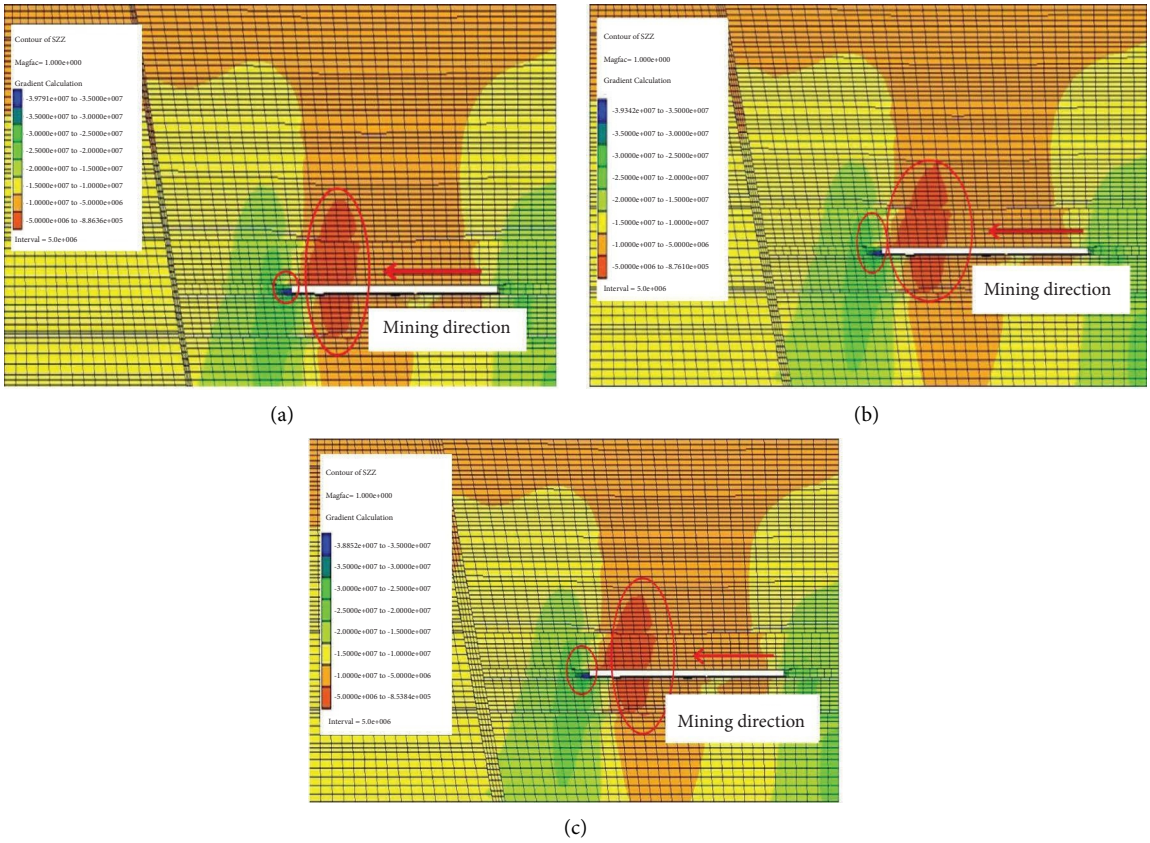

Figure 10: Vertical stress nephogram under three fault thicknesses for a 90 m distance. (a) 5 m. (b) 8 m. (c) 12 m.

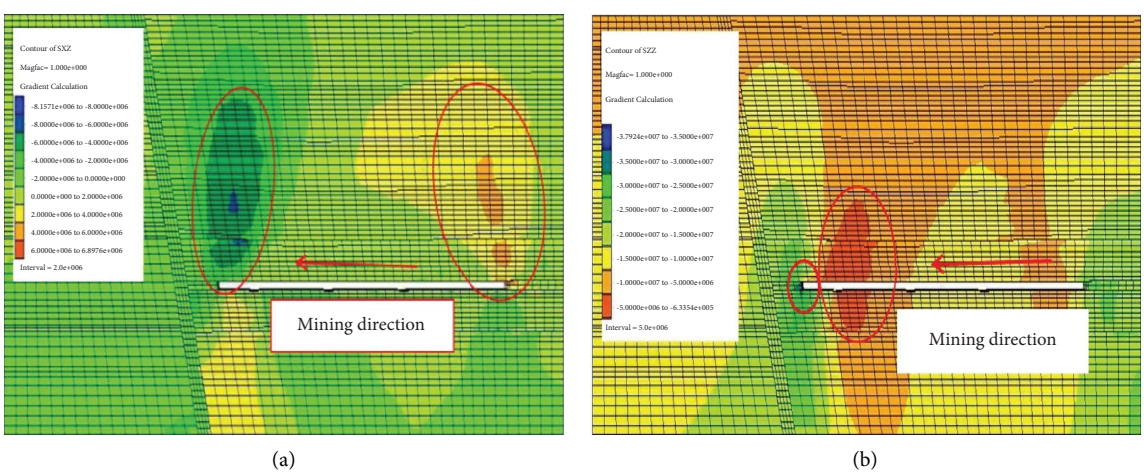

Figure 11: Shear stress and vertical stress nephogram of a 12 m fault at 30 m distance. (a) Shearing stress. (b) Normal stress.

4.2.4. Fault Seepage Characteristics. When the width of the fault is 12 m, the flow vector along the mining advancing fault is shown in Figure 19. The flow vector nephogram of the 5 m and 8 m fault fracture zones when the mining distance is 30 m is shown in Figure 20.

In Figure 19, when the distances between the working face and the fault are 210 m, 150 m, 90 m, and 30 m, the flow vector is 7.207 L, 9.637 L, 13.84 L, and 20.58 L, respectively. With the continuous advancement of the working face, the width of the corresponding coal pillar decreases. The plastic damage degree of the fault and the surrounding rock of the fault caused by mining are increasing, and the water pressure of the aquifer is also increasing. Finally, with the gradual decrease in the coal pillar width, the flow rate of water is gradually accelerated. Figure 20 shows that when the working face is mined to 30 m away from the fault, the flow rate of water increases due to the influence of the width of the fault fracture zone. This phenomenon proves that there is

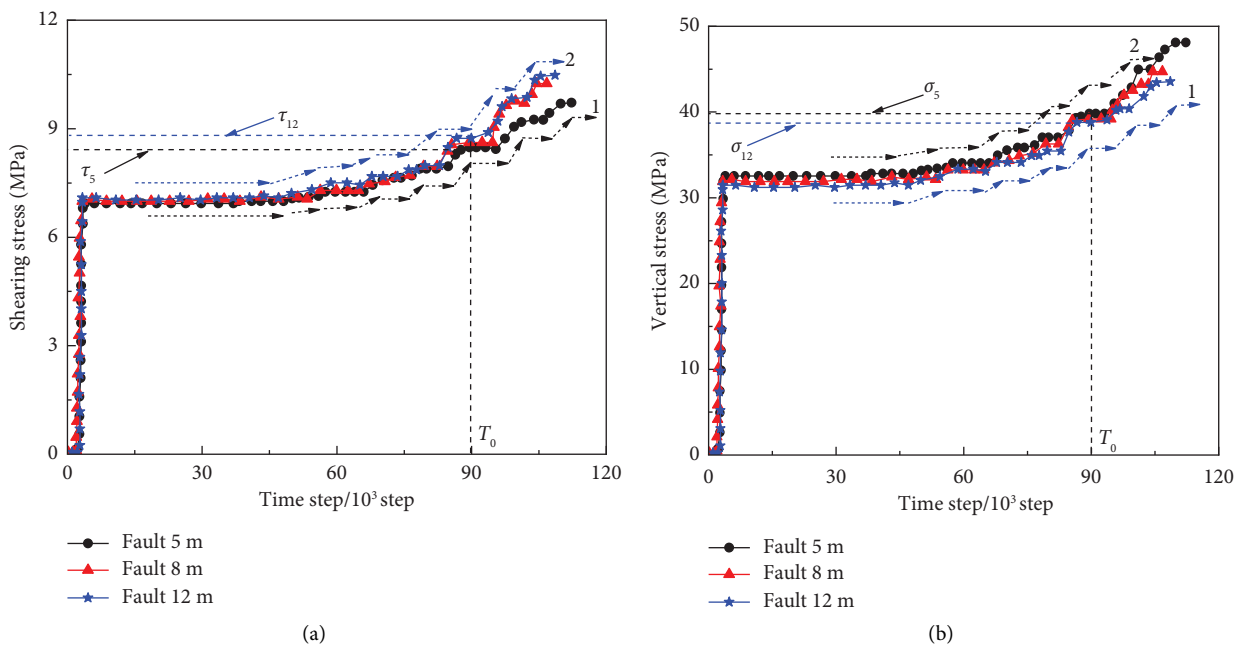

Figure 12: Shear stress and vertical stress curves of three faults at different advancing distances. (a) Shear stress. (b) Normal stress.

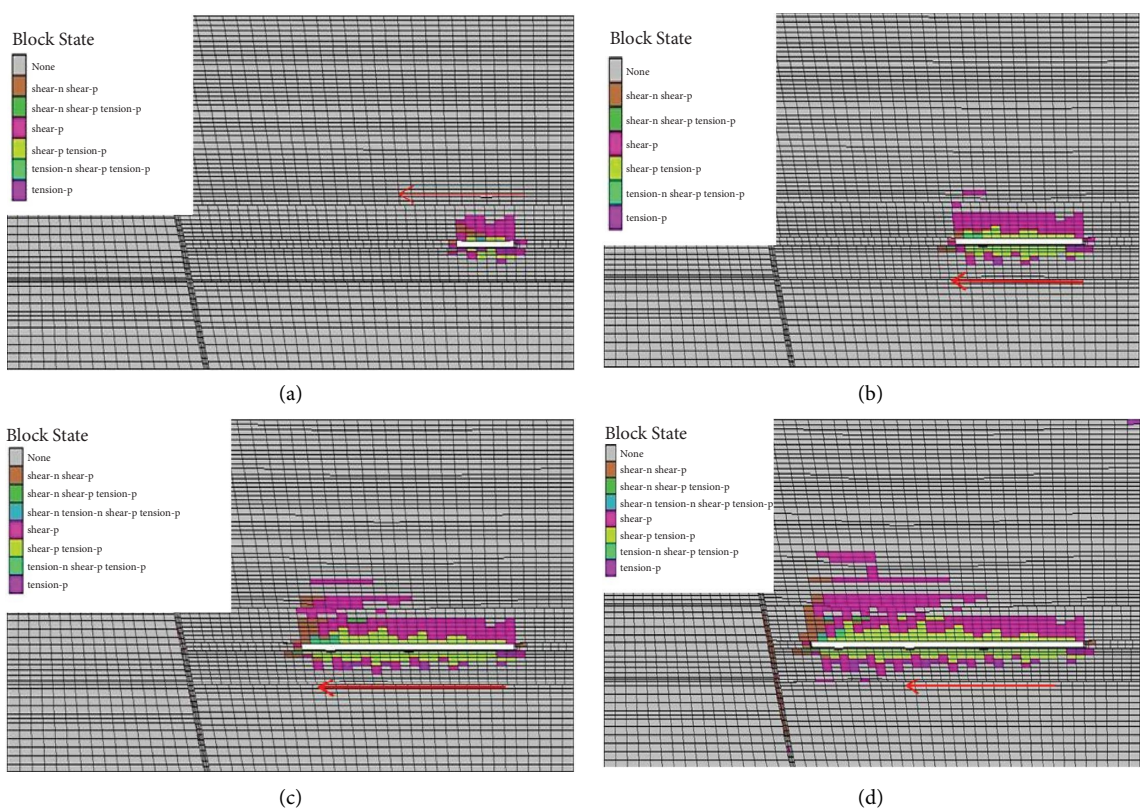

Figure 13: Plastic zone of the 5 m fault for three different distances. (a) 210 m. (b) 150 m. (c) 90 m. (d) 30 m.

a positive correlation between the risk of water inrush and the width of the fault fracture zone; that is, the risk of water inrush increases with the increase in the width of the fault fracture zone, and with the increase in the width of the fault fracture zone, the width of the safety pillar required for mining also increases accordingly.

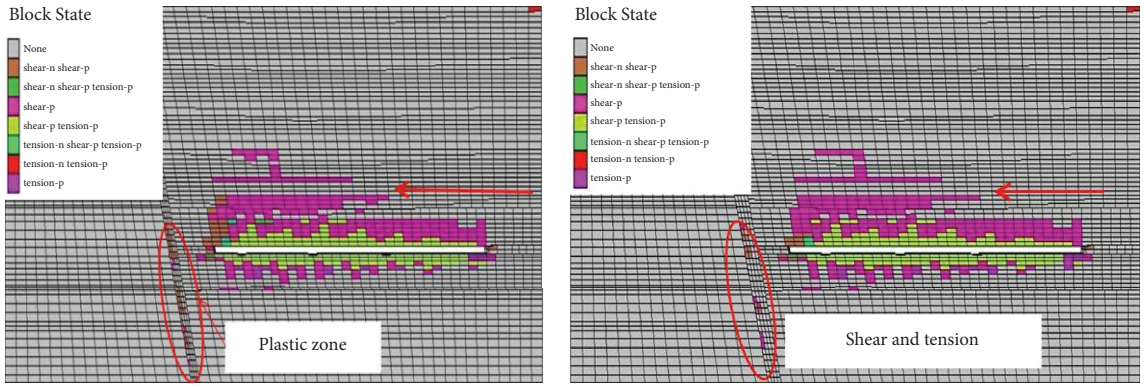

(a) (b)

Figure 14: Plastic zone of 8 m and 12 m fault for a 30 m distance. (a) 8 m. (b) 12 m.

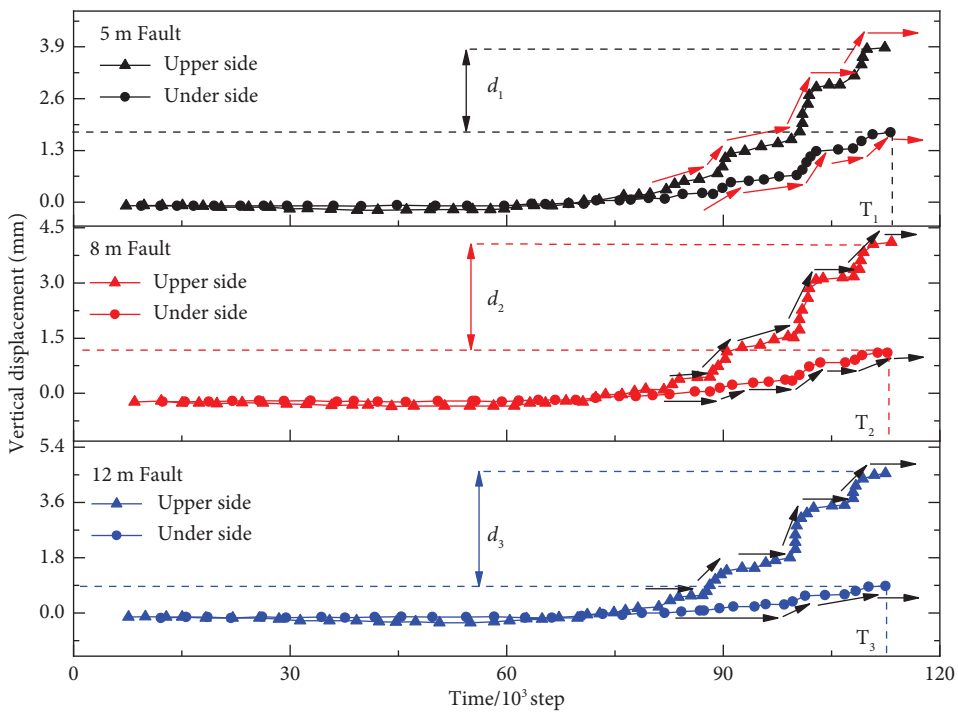

Figure 15: Displacement curve of the upper and lower plates of the fault.

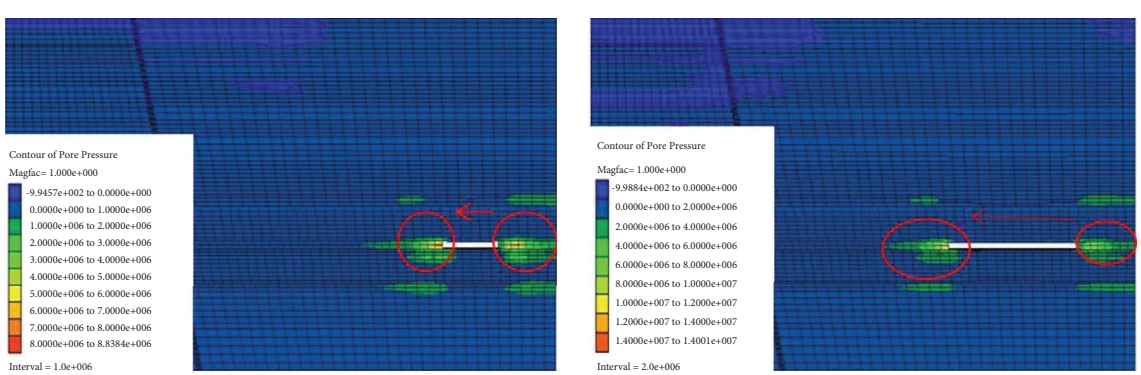

(a) (b)

Figure 16: Continued.

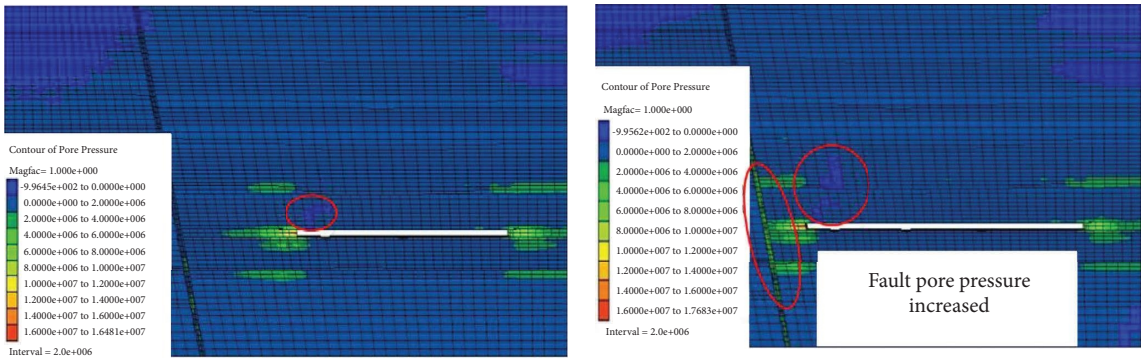

(c) (d)

Figure 16: Pore pressure of the 5 m fault under different propulsion distances. (a) 210 m. (b) 150 m. (c) 90 m fault. (d) 30 m fault.

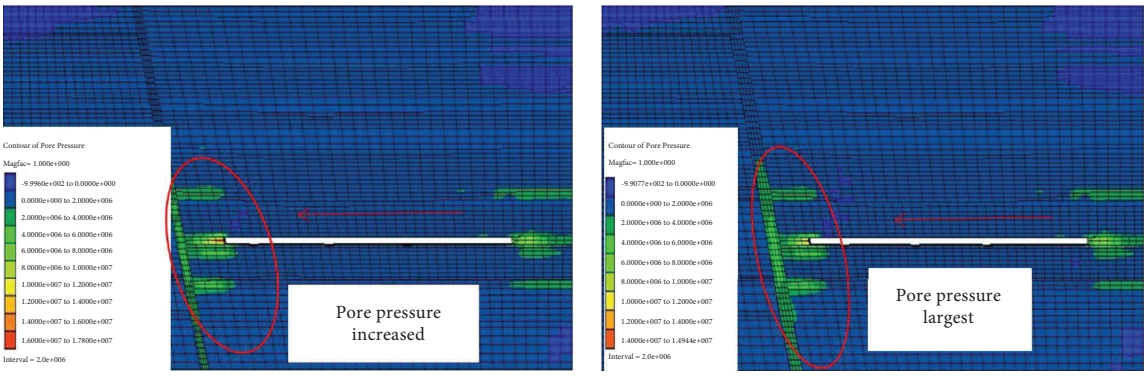

(a) (b)

Figure 17: Pore pressure change cloud chart of 8 m and 12 m faults for a 30 m distance between the mining face and fault. (a) 8 m fault. (b) 12 m fault.

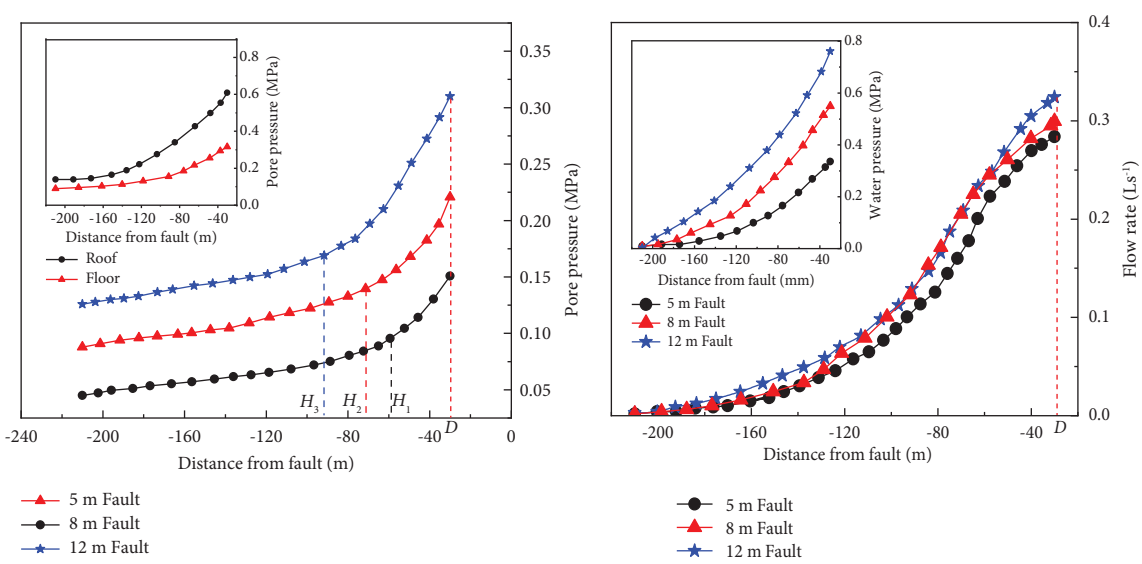

(a) (b)

Figure 18: Pore pressure and flow velocity of the faults under different mining advances. (a) Pore pressure. (b) Flow rate.

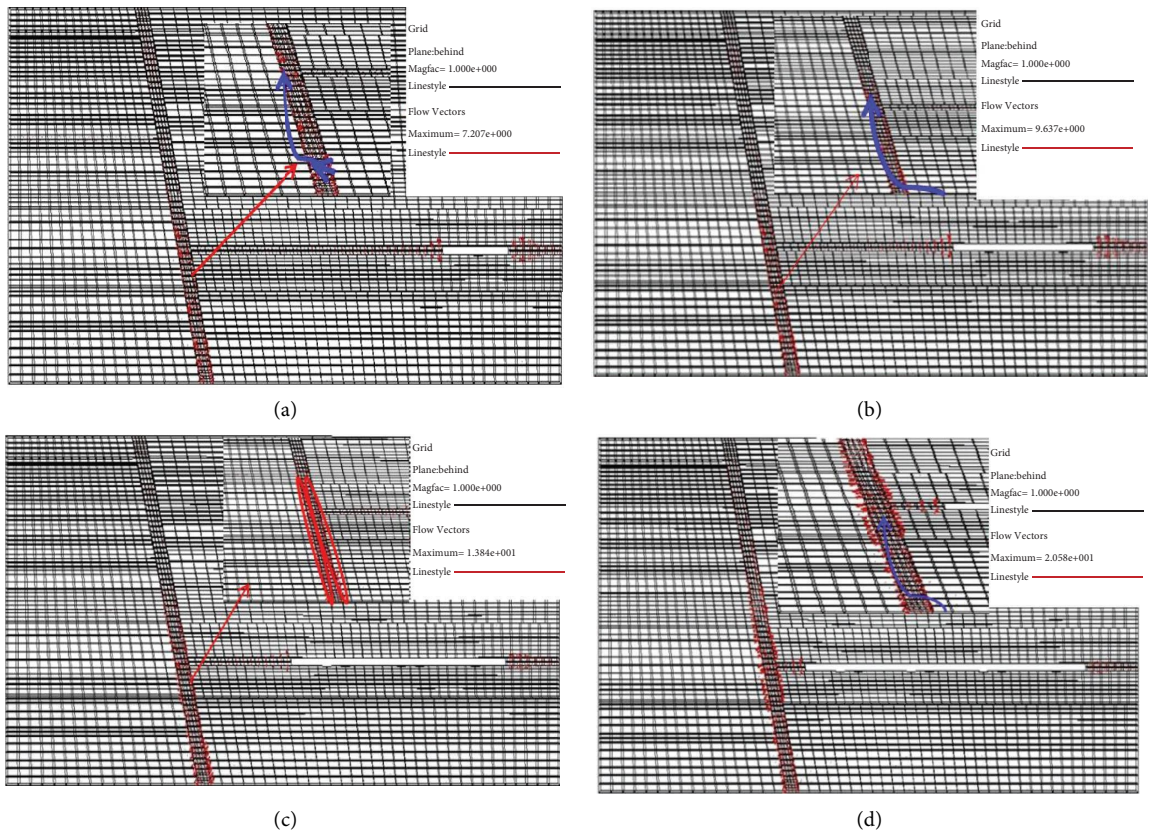

Figure 19: Flow vector diagram of the 12 m fault at different distances. (a) 210 m. (b) 150 m. (c) 90 m. (d) 30 m.

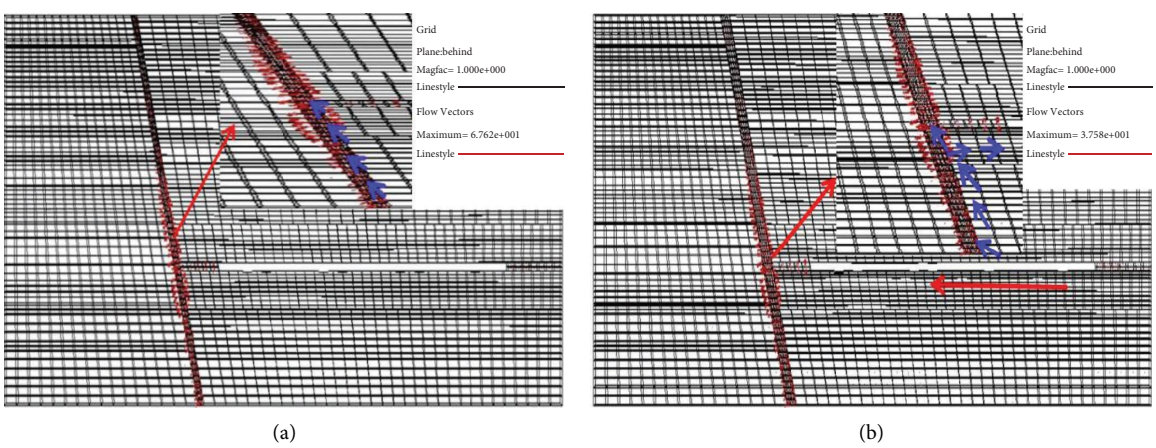

Figure 20: Flow vector diagrams of the 5 m and 8 m faults at 30 m mining. (a) 5 m fault. (b) 8 m fault.

5. Discussion

The recommended height of waterproof coal pillar in the #10 coal seam of Wugou coal mine obtained from three-zone theory and numerical model is shown in Table 5.

For the thickness of waterproof coal pillar, the theoretical calculation results are greater than the numerical model results, and the width of waterproof coal pillar increases with the increase of fault width. Therefore, for engineering applications, the theoretical calculation results

Table 5: Comparison of calculation results of waterproof coal pillar thickness.

The width of fault (m)	The height of waterproof coal pillar (m)	
	Three zone theory	Numerical model
5	62.6	60
8	72.3	71
12	94.2	93
Wugou mine	82.8	80.2

of the three zones are relatively safe, and the theoretical results of the three zones can be applied to engineering applications.

6. Conclusions

During coal seam mining, groundwater enters the excavation face through faults, and the water inrush disaster caused by the tunnel face is the main problem faced by mining near confined water. The engineering practice shows that the reasonable thickness of waterproof coal pillar in front of the tunnel face is an effective method to solve this problem. Based on the mining background of Wugou coal mine, this paper establishes the mechanical model of waterproof coal pillar, analyses the mechanical properties and water conductivity of faults under different excavation distances and fault thicknesses, and obtains the calculation model of three-zone waterproof thickness. Finally, the rationality of the calculation results is verified by the numerical model results. The main conclusions are as follows:

(1) Comparing the three-zone theory and numerical model, it is concluded that the width of waterproof coal pillar is positively correlated with the influence depth of fault and water pressure. When mining advances, the tangential stress and normal stress increase. In front of the working face, the normal stress is tensile stress, and the compressive stress is at the roof and floor. However, the peak value of tangential stress mainly appears at both ends of the excavation face, and it shows compression-shear failure at the initial section and tensile-shear failure at the mining end.

(2) The pore water pressure and flow rate increase nonlinearly with the increasing mining distance and fault thickness, with peak values of 0.8 MPa and 0.35 L/s for a fault width of 12 m. The peak value of the upper and lower plates of the fault increases sharply, which means that fault activation occurs and a water rush channel is formed.

(3) The comparison of theoretical and numerical simulations indicates that when the mining distance approaches the fault, a reasonable waterproof coal pillar can effectively control the occurrence of water inrush, and the numerical simulation results of coal pillar width are larger than theoretical values in three regions. In this study, the recommended thickness of the waterproof coal pillar in the No. 1011 working face of the Wugou coal mine is 80.2 m.

(4) The three-zone theoretical model in this paper provides a reasonable solution for the study of waterproof coal pillars, which is helpful to understand the hydraulic change process of the rock strata on the working face during near-fault mining, and can be used as an auxiliary measure to prevent and control water disasters on the excavation face. However, further research is needed on the water inrush mechanism of the fault tectonic zone and the countermeasures for the prevention and control of water on the working face.

Data Availability

The datasets generated and analysed during the current study are not publicly available due to continuous studying but are available from the corresponding author on reasonable request.

Conflicts of Interest

The authors declare that they have no conflicts of interest.

Authors' Contributions

Y.Q.W. wrote the main manuscript text, B.S.Y. guide the theme and theory of the manuscript, and J.Z. prepared Figures 8–14. All authors reviewed the manuscript.

Acknowledgments

This research was supported by the Qingdao Huanghai University Doctoral Research Foundation. The authors thank AJE (https://www.aje.com/) for English language editing and review services.

References

[1] M. R. Islam and R. Shinjo, "Mining-induced fault reactivation associated with the main conveyor belt roadway and safety of the Barapukuria Coal Mine in Bangladesh: constraints from BEM simulations," *International Journal of Coal Geology*, vol. 79, no. 4, pp. 115–130, 2009.

[2] J. W. Lamoreaux, Q. Wu, and Z. Wanfang, "New development in theory and practice in mine water control in China," *Carbonates and Evaporites*, vol. 29, no. 2, pp. 141–145, 2014.

[3] Z. Liang, W. Song, and W. Liu, "Theoretical models for simulating the failure range and stability of inclined floor strata induced by mining and hydraulic pressure," *International Journal of Rock Mechanics and Mining Sciences*, vol. 132, Article ID 104382, 2020.

[4] A. J. Das, P. K. Mandal, S. P. Sahu, A. Kushwaha, R. Bhattacharjee, and S. Tewari, "Evaluation of the effect of fault on the stability of underground workings of coal mine through DEM and statistical analysis," *Journal of the Geological Society of India*, vol. 92, no. 6, pp. 732–742, 2018.

[5] L. J. Donnelly, "A review of coal mining induced fault reactivation in Great Britain," *The Quarterly Journal of Engineering Geology and Hydrogeology*, vol. 39, no. 1, pp. 5–50, 2006.

[6] P. Bukowski, "Water hazard assessment in active shafts in upper silesian coal basin mines," *Mine Water and the Environment*, vol. 30, no. 4, pp. 302–311, 2011.

[7] A. Sainoki, H. S. Mitri, D. Chinnasane, and A. K. Schwartzkopff, "Quantitative energy-based evaluation of the intensity of mining-induced seismic activity in a fractured rock mass," *Rock Mechanics and Rock Engineering*, vol. 52, no. 11, pp. 4651–4667, 2019.

[8] Q. Zhou, J. Herrera, and A. Hidalgo, "The numerical analysis of fault-induced mine water inrush using the extended finite element method and fracture mechanics," *Mine Water and the Environment*, vol. 37, no. 1, pp. 185–195, 2018.

[9] M. R. Daryono, D. H. Natawidjaja, B. Sapiie, and P. Cummins, "Earthquake geology of the lembang fault, west java, Indonesia," *Tectonophysics*, vol. 751, pp. 180–191, 2019.

[10] Y. G. Xue, G. K. Li, X. K. Wang, W. M. Yang, D. H. Qiu, and M. X. Su, "Analysis and optimization design of submarine tunnels crossing fault fracture zones based on numerical simulation," *Marine Georesources and Geotechnology*, vol. 38, no. 9, pp. 1106–1117, 2020.

[11] K. K. A. K. Ersoy, "A comparative assessment of indirect methods for estimating the uniaxial compressive and tensile strength of rocks," *Arabian Journal of Geosciences*, vol. 4, no. 8, pp. 2393–2403, 2014.

[12] A. Sainoki and H. S. Mitri, "Effect of slip-weakening distance on selected seismic source parameters of mining-induced fault-slip," *International Journal of Rock Mechanics and Mining Sciences*, vol. 73, pp. 115–122, 2015.

[13] A. Gudmundsson, S. S. Berg, K. B. Lyslo, and E. &Skurtveit, "Fracture networks and fluid transport in active fault zones," *Journal of Structural Geology*, vol. 23, no. 2-3, pp. 343–353, 2001.

[14] W. R. Bailey, J. J. Walsh, and T. Manzocchi, "Fault populations, strain distribution and basement fault reactivation in the East Pennines Coalfield, UK," *Journal of Structural Geology*, vol. 27, no. 5, pp. 913–928, 2005.

[15] A. Fakhimi, Q. Lin, and J. F. Labuz, "Insights on rock fracture from digital imaging and numerical modeling," *International Journal of Rock Mechanics and Mining Sciences*, vol. 107, pp. 201–207, 2018.

[16] M. Rehbock-Sander and T. Jesel, "Fault induced rock bursts and micro-tremors-experiences from the Gotthard Base Tunnel," *Tunnelling and Underground Space Technology*, vol. 81, pp. 358–366, 2018.

[17] E. Pilecka and D. Szwarkowski, "The influence of the fault zone width on land surface vibrations after the high-energy tremor in the Rydułtowy-Anna hard coal mine," *E3S Web of Conferences*, vol. 36, p. 02007, 2018.

[18] A. Sainoki and H. S. Mitri, "Quantitative analysis with plastic strain indicators to estimate damage induced by fault-slip," *Journal of Rock Mechanics and Geotechnical Engineering*, vol. 10, no. 1, pp. 1–10, 2018.

[19] L. Qiu, D. Song, Z. Li, B. Liu, and J. Liu, "Research on AE and EMR response law of the driving face passing through the fault," *Safety Science*, vol. 117, pp. 184–193, 2019.

[20] O. Sammarco and D. Eng, "Spontaneous inrushes of water in underground mines," *International Journal of Mine Water*, vol. 5, no. 3, pp. 29–41, 1986.

[21] W. Sun, Y. Xue, T. Li, and W. Liu, "Multi-field coupling of water inrush channel formation in a deep mine with a buried fault," *Mine Water and the Environment*, vol. 38, no. 3, pp. 528–535, 2019.

[22] H. W. Wang, R. M. Shi, D. X. Deng, Y. D. Jiang, G. Wang, and W. L. Gong, "Characteristic of stress evolution on fault surface and coal bursts mechanism during the extraction of longwall face in Yima mining area, China," *Journal of Structural Geology*, vol. 136, Article ID 104071, 2020.

[23] M. F. Howladar, "Coal mining impacts on water environs around the Barapukuria coal mining area, Dinajpur, Bangladesh," *Environmental Earth Sciences*, vol. 70, no. 1, pp. 215–226, 2013.

[24] W. Song and Z. Liang, "Theoretical and numerical investigations on mining-induced fault activation and groundwater outburst of coal seam floor," *Bulletin of Engineering Geology and the Environment*, vol. 80, no. 7, pp. 5757–5768, 2021.

[25] B. Azarfar, S. Ahmadvand, J. Sattarvand, and B. Abbasi, "Stability analysis of rock structure in large slopes and open-pit mine: numerical and experimental fault modeling," *Rock Mechanics and Rock Engineering*, vol. 52, no. 12, pp. 4889–4905, 2019.

[26] G. F. Hofmann and L. J. Scheepers, "Simulating fault slip areas of mining induced seismic tremors using static boundary element numerical modelling," *Mining Technology*, vol. 120, no. 1, pp. 53–64, 2013.

[27] J. Sjöberg, F. Perman, C. Quinteiro, L. Malmgren, C. Dahner-Lindkvist, and M. Boskovic, "Numerical analysis of alternative mining sequences to minimise potential for fault slip rockbursting," *Mining Technology*, vol. 121, no. 4, pp. 226–235, 2012.

[28] A. Sainoki, H. S. Mitri, and D. Chinnasane, "Characterization of aseismic fault-slip in a deep hard rock mine through numerical modelling: case study," *Rock Mechanics and Rock Engineering*, vol. 50, no. 10, pp. 2709–2729, 2017.

[29] Y. Potvin, J. Jarufe, and J. Wesseloo, "Interpretation of seismic data and numerical modelling of fault reactivation at El Teniente, Reservas Norte sector," *Mining Technology*, vol. 119, no. 3, pp. 175–181, 2013.

[30] A. Sainoki and H. S. Mitri, "Effect of fault-slip source mechanism on seismic source parameters," *Arabian Journal of Geosciences*, vol. 9, no. 1, pp. 12–69, 2016.

[31] A. Sainoki and H. S. Mitri, "Dynamic behaviour of mining-induced fault slip," *International Journal of Rock Mechanics and Mining Sciences*, vol. 66, pp. 19–29, 2014.

[32] B. H. Kim and M. K. Larson, "Development of a fault-rupture environment in 3d: a numerical tool for examining the mechanical impact of a fault on underground excavations," *International Journal of Mining Science and Technology*, vol. 29, no. 1, pp. 105–111, 2019.

[33] S. W. Quan, P. Kong, Q. L. Wu, X. G. Xu, X. Y. Wu, and T. &Guo, "Study on overburden rock movement and stress distribution characteristics under the influence of a normal fault," *Advances in Civil Engineering*, vol. 2020, Article ID 7859148, 16 pages, 2020.